remote sensing

MDPI

Article

Characteristics of the Global Radio Frequency Interference in the Protected Portion of L-Band

Mustafa Aksoy [1,*], Hamid Rajabi [2], Pranjal Atrey [3] and Imara Mohamed Nazar [1]

[1] Department of Electrical and Computer Engineering, University at Albany—State University of New York, Albany, NY 12222, USA; imohamednazar@albany.edu
[2] Department of Electrical Engineering and Computer Science, University of California, Merced, CA 95343, USA; hrajabi2@ucmerced.edu
[3] Department of Computer Science, University at Albany—State University of New York, Albany, NY 12222, USA; patrey2@albany.edu
* Correspondence: maksoy@albany.edu; Tel.: +1-518-442-2597

Abstract: The National Aeronautics and Space Administration's (NASA's) Soil Moisture Active–Passive (*SMAP*) radiometer has been providing geolocated power moments measured within a 24 MHz band in the protected portion of L-band, i.e., 1400–1424 MHz, with 1.2 ms and 1.5 MHz time and frequency resolutions, as its Level 1A data. This paper presents important spectral and temporal properties of the radio frequency interference (*RFI*) in the protected portion of L-band using *SMAP* Level 1A data. Maximum and average bandwidth and duration of *RFI* signals, average *RFI*-free spectrum availability, and variations in such properties between ascending and descending satellite orbits have been reported across the world. The average bandwidth and duration of individual *RFI* sources have been found to be usually less than 4.5 MHz and 4.8 ms; and the average *RFI*-free spectrum is larger than 20 MHz in most regions with exceptions over the Middle East and Central and Eastern Asia. It has also been shown that, the bandwidth and duration of *RFI* signals can vary as much as 10 MHz and 10 ms, respectively, between ascending and descending orbits over certain locations. Furthermore, to identify frequencies susceptible to *RFI* contamination in the protected portion of L-band, observed *RFI* signals have been assigned to individual 1.5 MHz *SMAP* channels according to their frequencies. It has been demonstrated that, contrary to common perception, the center of the protected portion can be as *RFI* contaminated as its edges. Finally, there have been no significant correlations noted among different *RFI* properties such as amplitude, bandwidth, and duration within the 1400–1424 MHz band.

Keywords: radio frequency interference; microwave radiometry; Soil Moisture Active Passive; L-band

Citation: Aksoy, M.; Rajabi, H.; Atrey, P.; Mohamed Nazar, I. Characteristics of the Global Radio Frequency Interference in the Protected Portion of L-Band. *Remote Sens.* **2021**, *13*, 253. https://doi.org/10.3390/rs13020253

Received: 15 December 2020
Accepted: 11 January 2021
Published: 13 January 2021

1. Introduction

The protected portion of L-band, i.e., between 1400 and 1427 MHz, has been solely allocated for passive radio astronomy and Earth exploration remote sensing applications [1]. However, significant radio frequency interference (*RFI*) contamination due to illegal transmitters radiating within this spectrum and out-of-band emissions leaking from adjacent bands has been reported in measurements of L-band microwave radiometers deployed in spaceborne remote sensing missions [2,3]. Such *RFI* contamination, if not detected and mitigated, may degrade the quality of radiometric data to be used in the retrieval of important geophysical parameters such as soil moisture, sea surface salinity, sea surface wind, and vegetation index; thus, several *RFI* detection and mitigation algorithms have been developed and implemented in L-band microwave radiometers to address the problem [4]. Pulse blanking techniques in time and frequency domains [5,6], kurtosis and other normality tests [7–10], polarimetric techniques [11], and spatial domain *RFI* detection methods [12] are some of these algorithms discussed thoroughly in the literature.

The National Aeronautics and Space Administration's (NASA) Soil Moisture Active–Passive (*SMAP*) mission is one of the most recent spaceborne remote sensing missions, which carries a radiometer, operating within the protected portion of L-band, i.e., 1400–1424 MHz, to measure brightness temperatures in horizontal and vertical polarizations from the Earth's surface to retrieve soil moisture with an acceptable accuracy and uncertainty [13,14]. Unlike previous L-band radiometers, however, the *SMAP* radiometer includes a digital backend that allows calculating radiometer signal moments in both polarizations as well as their correlations with unprecedented time and frequency resolutions of 1.2 ms and 1.5 MHz, respectively [15].

The signal moments and correlations generated by *SMAP*'s radiometer digital backend enable a multi-domain comprehensive *RFI* detection and mitigation procedure, which consists of time domain pulse blanking, cross-frequency detection, kurtosis, and polarimetric *RFI* detection algorithms. As ground processing, these *RFI* detection algorithms are simultaneously applied to signal moments and correlations; and, to maximize the probability of *RFI* detection, flags created by each individual algorithm are combined with a logical "OR" operator. This so-called "maximum probability of detection (MPD)" approach is shown to be capable of detecting and mitigating a significant fraction of the *RFI* contamination in the protected portion of L-band at the expense of high false-alarm rates [16].

Besides its efficacy to detect and mitigate *RFI*, *SMAP* also allows characterization of the *RFI* environment in the protected portion of L-band in terms of its temporal, spectral, and spatial properties using the geolocated outputs of the *SMAP* digital backend. These properties determine the performance of *RFI* detection and mitigation algorithms implemented in microwave radiometry; thus, such characterization is essential for future L-band remote sensing missions. In [17], authors have presented an initial analysis of *RFI* characteristics in the protected portion of L-band using *SMAP*'s Level 1A data, i.e., signal moments and correlations produced by its digital backend, which investigated overall *RFI* bandwidth, duration, and center frequencies for the world as a whole. However, spectrum allocations and usage can be different in different regions and times; thus, further analyses of the *RFI* properties based on their geographical location and observation times are required. This paper, expanding on a short conference paper presented at the 2019 IEEE International Geoscience and Remote Sensing Symposium [18], addresses this gap in the literature and is structured as follows:

- A short review of *SMAP*, its radiometer data, and the *RFI* presence in its radiometer measurements are given in Section 2.
- An *RFI* detection and characterization procedure, similar to the one discussed in [17,18] with some improvements, applied to *SMAP* Level 1A data measured between May 1 and 7, 2019 to extract *RFI* properties in the protected portion of L-band is presented in Section 3. The multi-domain procedure contains time and frequency domain pulse blanking, kurtosis, and skewness algorithms implemented simultaneously. Then, similar to the *SMAP* data processing, detection results from individual algorithms are combined with a logical "OR" operator.
- Based on detection results, geo-located characteristics of the L-band *RFI* environment such as the maximum and average *RFI* bandwidth and duration, average *RFI*-free bandwidth, and the variance in such properties between ascending and descending *SMAP* observations are discussed in Section 4. This section also mentions specific frequencies in the protected portion of L-band susceptible to *RFI* in different geographic regions.
- Finally, Section 5 discusses the results and provides insight for future L-band microwave radiometry missions regarding required *RFI* detection and mitigation capabilities.

2. *SMAP* Data and *RFI* Presence in L-Band

NASA's Soil Moisture Active–Passive (*SMAP*) radiometer, owing to its onboard digital backend, provides data from space resolved in both time and frequency within the 1400–1424 MHz spectrum; thus, allowing the retrieval of temporal, spectral, and spatial properties of the *RFI* environment in the protected portion of L-band. The digital back-

end produces signal moments and their correlations in full-band, i.e., in a 1 × 24 MHz frequency channel with 300 μs time resolution, and in sub-band, i.e., in 16 × 1.5 MHz frequency channels with 1.2 ms time resolution [15]. These moments in both horizontal and vertical polarizations along with their corresponding geo-location information are stored in publicly available *SMAP* Level 1A files [19]. The *SMAP* Level 1B processor first calibrates Level 1A data to obtain brightness temperatures, then implements a multi-domain *RFI* detection and mitigation procedure that includes time domain pulse blanking (in full-band), cross-frequency detection (in sub-band), kurtosis (in both full-band and sub-band), and polarimetric (in both full-band and sub-band) algorithms. *RFI* flags of all detectors are combined with logical "OR" operator to maximize the probability of detection, and *RFI*-free measurements in sub-band are averaged over time and frequency within each radiometer footprint to create *RFI*-mitigated brightness temperature products [20]. *SMAP* Level 1B data, also publicly available online [21], contain brightness temperature measurements before and after *RFI* mitigation, and their differences demonstrate the amplitude of the detected *RFI* contamination.

Figure 1a,b demonstrates the maximum horizontally polarized (H-pol) brightness temperatures measured by *SMAP* over 0.25° × 0.25° latitude × longitude grid cells before and after *RFI* mitigation across the world between May 1 and 7, 2019. It can be seen that, although most of the *RFI* contamination is successfully removed, some *RFI* corruption can still be seen even after *RFI* mitigation. Such persistent *RFI*, present mostly over Japan and some metropolitan areas in Europe, Middle East and China, is reported to be long-duration and wideband "noise-like" interference, which cannot be easily detected by the *SMAP* algorithms [22].

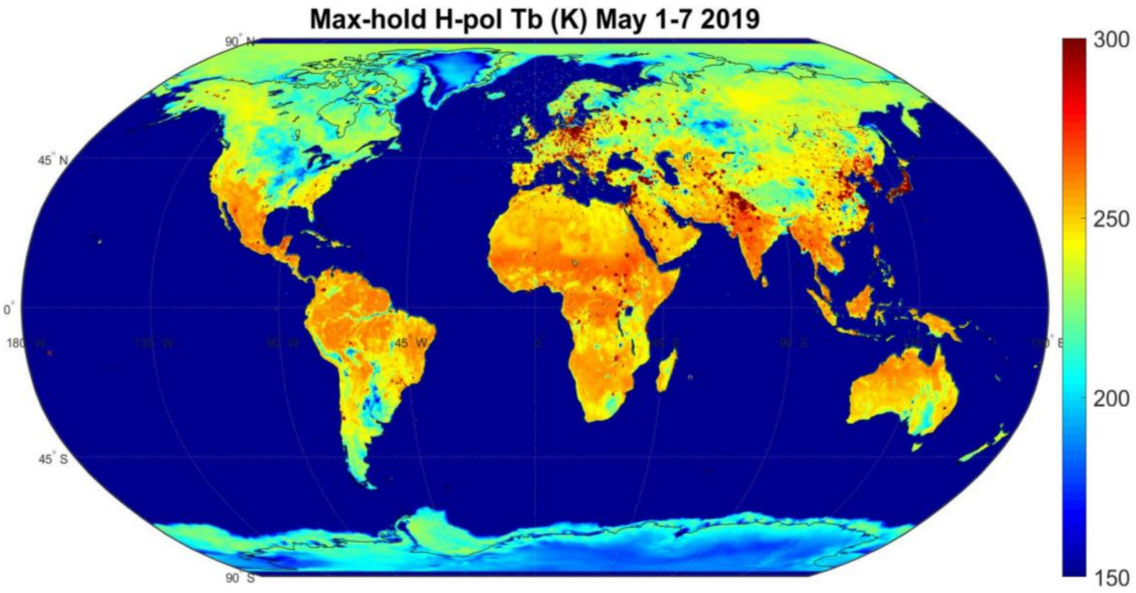

(**a**)

Figure 1. *Cont.*

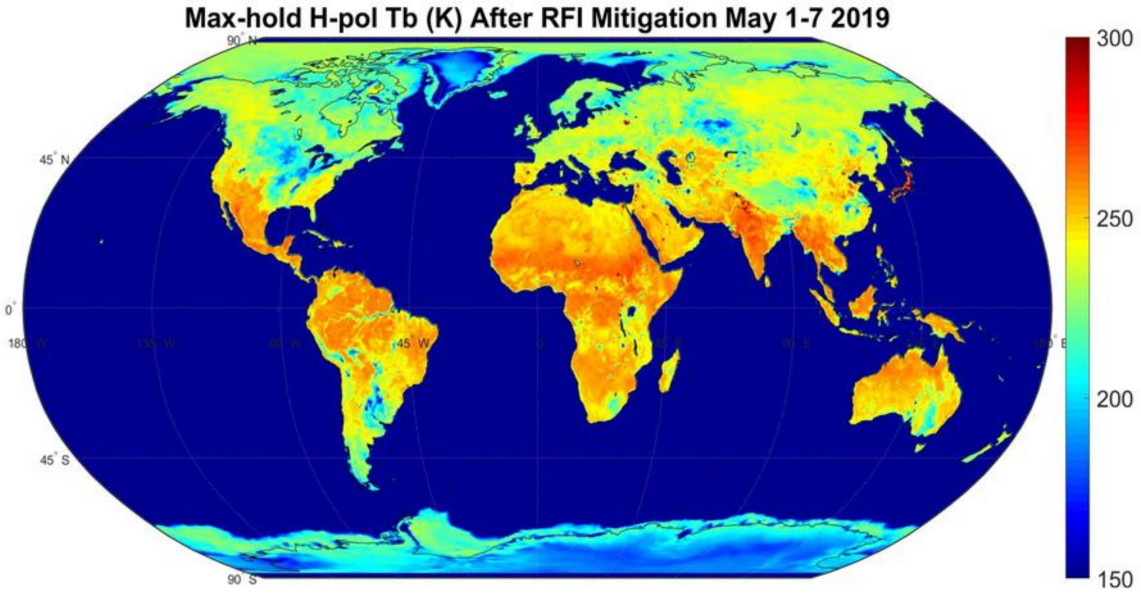

(**b**)

Figure 1. Soil Moisture Active–Passive (*SMAP*) Max-hold horizontally polarized (H-pol) brightness temperatures between 1 and 7 May 2019 (**a**) before and (**b**) after radio frequency interference (*RFI*) mitigation on 0.25° × 0.25° gridded maps.

Figure 2, on the other hand, shows the maximum *RFI* amplitude, i.e., the maximum difference between original and *RFI*-mitigated H-pol brightness temperatures. The figure indicates a significant, worldwide *RFI* problem for L-band microwave radiometry, which is especially severe over Europe and Eastern Asia. Vertically polarized (V-pol) *RFI* amplitudes are not shown here but are very similar. It is important to note that brightness temperature values are limited not to exceed 340 K in *SMAP* Level 1B data, which may result in the underestimation of *RFI* amplitudes in certain locations with severe contamination. Moreover, since noise-like *RFI* cannot be properly detected by *SMAP*, *RFI* amplitudes where such interference exists are much lower than their true values.

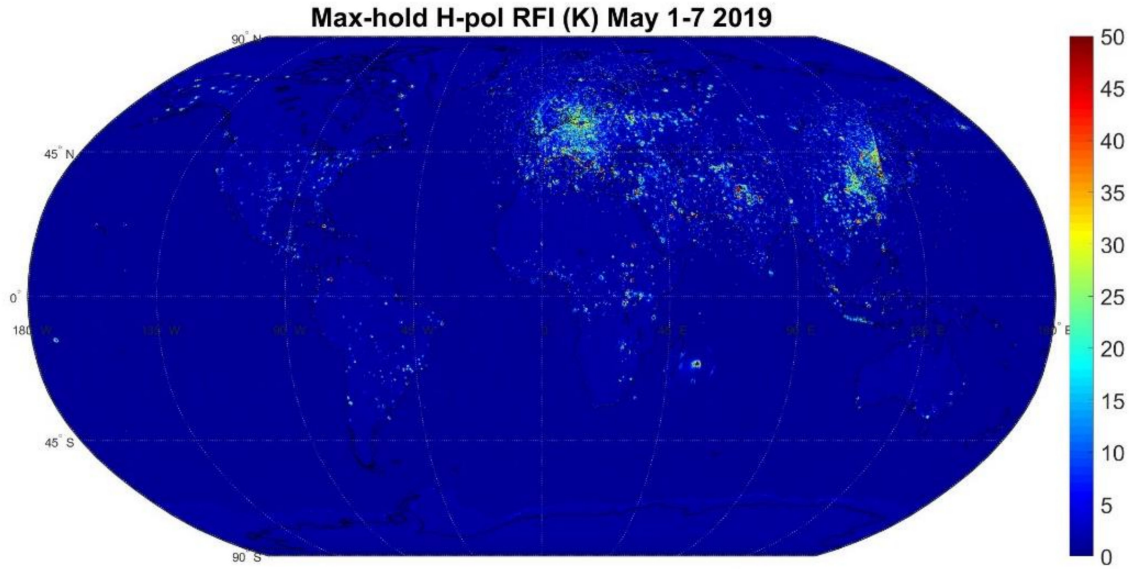

Figure 2. Max-hold H-pol *RFI* amplitudes, i.e., the difference between brightness temperatures before and after *RFI* mitigation, between 1 and 7 May 2019. The results demonstrate significant *RFI* presence in the protected portion of L-band, especially over Europe and Eastern Asia.

SMAP Level 1B data provide valuable information regarding *RFI* presence and amplitudes; however, since these brightness temperature products are averaged over radiometer footprints (24 MHz and 9.6 ms), they do not reveal the temporal and spectral properties of the *RFI* contamination. Thus, in the following sections, *SMAP* Level 1A data resolved in time and frequency are analyzed to demonstrate these properties.

3. Approach to Reveal L-Band *RFI* Characteristics

Temporal and spectral properties of L-band *RFI* can be obtained by applying detection algorithms to publicly available *SMAP* Level 1A radiometer products. An alternative approach would be analyses of official *SMAP RFI* flags, resolved in time and frequency, generated by the *SMAP* Level 1B processor; however, such information is not publicly available. Thus, the *RFI* detection procedure described in this section and the resulting *RFI* flags may not be exactly the same as the official *SMAP* products.

Similar to [17,18], the *RFI* detection and characterization process of this study starts with preprocessing of the Level 1A data, and then, four different *RFI* detection algorithms, i.e., cross frequency, time domain pulse blanking, kurtosis, and skewness, are applied to retrieve the properties of *RFI* observed by *SMAP*. Note that, unlike *SMAP*, polarimetry is not used to detect *RFI* in this study. Below, this process is explained step by step.

3.1. Step I: Statistics Calculations

Kurtosis, skewness, and power (2nd moment) of the sub-band data in each Level 1A file are calculated using the provided signal moments and organized as matrices where rows represent the 16 × 1.5 MHz channels and columns represent 1.2 ms sub-band time packets (the matrices are calculated for in-phase and quadrature components of the radiometer counts separately, then averaged).

3.2. Step II: Cross-Frequency Algorithm

The cross-frequency detection algorithm is applied across the 16 sub-band channels for each 1.2 ms sub-band time packet in the power matrices after the matrices are normalized over the 24 MHz bandwidth using their *median* values. Then, *i*th sub-band channel is flagged as *RFI* contaminated when

$$|P_i - P_{median}| > 3 \times MAD \quad (1)$$

where $MAD = median\ (|P_i - P_{median}|)$, and P_i and P_{median} denote the power of the *i*th frequency channel in a 1.2 ms time packet and *median* power of that packet, respectively. This algorithm is the same as the cross-frequency algorithm presented in [17] but differs from *SMAP*, which uses mean power and standard deviation instead of *median* power and *median* absolute deviation to determine the detection threshold [20]. Use of *median* and *median* absolute deviation of power is preferred in this study as the mean and standard deviation values have been found susceptible to bias in the case of *RFI* presence.

Note that, the cross-frequency algorithm is efficient against *RFI* signals with limited bandwidths as wideband *RFI* may distort the *median* value across the 16 channels and lead to biased thresholds.

3.3. Step III: Time Domain Pulse Blanking Algorithm

The time domain pulse blanking algorithm implements a similar thresholding across 10-*SMAP*-footprint-long sliding windows for each sub-band channel in the power matrices. In comparison to the time domain thresholding implemented in [17] across 0.4-*SMAP*-scan-long windows (~96 footprint long), shorter sliding windows are preferred in this study so that biases in coastal regions due to significant brightness temperature differences between aquatic and dry regions can be avoided. *RFI* flagging is again based on Equation (1), where this time P_i and P_{median} are the *i*th power sample in a sliding window and the *median* power of that window, respectively. Note that this algorithm is again different than *SMAP* as it

uses *median* and *median* absolute deviation of the measured power instead of its mean and standard deviation.

The time domain algorithm would be efficient in the case of *RFI* contamination with durations much shorter than the thresholding window used by the algorithm, i.e., 10 *SMAP* footprints.

3.4. Step IV: Kurtosis Algorithm

The kurtosis detection algorithm flags *RFI*, in the kurtosis matrices, when a kurtosis sample significantly deviates from the nominal expected *RFI*-free kurtosis value, which was assumed to be 3 [21]. This procedure can be mathematically formulated as follows:

$$|K - 3| > \beta_k \sigma_k \tag{2}$$

where K denotes a measured kurtosis value in the kurtosis matrices; β_k is the threshold coefficient, which is selected to be 3 in this study; and σ_k is the standard deviation of the *RFI*-free kurtosis samples, which can be calculated as described in [17]. This algorithm is the same as the kurtosis algorithm implemented in *SMAP* [20], and the value of β_k is selected to set the false alarm rate to 0.3% for this algorithm in *RFI*-free measurements. β_k can be decreased if better detection performance is desired at the expense of higher false-alarm rates, or it can be increased if lower false-alarm rates are targeted.

Although the kurtosis algorithm is capable of detecting all non-Gaussian *RFI* signals, it is reported to be much more sensitive against short-duty-cycle interference [23].

3.5. Step V: Skewness Algorithm

The skewness algorithm performs a thresholding procedure similar to the kurtosis thresholding in the skewness matrices as follows:

$$|S - S_{nom}| > \beta_s \sigma_s \tag{3}$$

where S is a skewness value in the skewness matrices; S_{nom} denotes the expected skewness value for *RFI*-free measurements, which is assumed to be 0; β_s is the thresholding coefficient, which again is set to 3; and σ_s is the standard deviation of *RFI*-free skewness values which can be calculated as mentioned in [17]. This algorithm, the same as described in [17], is not implemented in *SMAP*, and the thresholding selection again sets the false-alarm rate to 0.3% in *RFI*-free cases for the skewness algorithm.

The skewness algorithm searches for asymmetry in the probability distribution function of the radiometer measurements as an indication for *RFI* contamination [24]. Thus, it is important to note that, since long-duration and constant-amplitude *RFI* signals that occupy the entire 1.2 ms sub-band time packets shift the overall distribution without spoiling the symmetry, the skewness algorithm is not very efficient against them.

3.6. Step VI: MPD Flags

Similar to what is implemented in *SMAP* Level 1B processing [20], the outputs, i.e., *RFI* flags, of the individual detectors described in Steps II–V are combined through a logical "OR" operation as maximum probability of detection (MPD) flags. This procedure increases the false-alarm rate; however, since this study mainly aims to characterize the *RFI* properties, increased radiometric data loss due to higher false-alarm rates is considered acceptable to obtain the maximum probability of *RFI* detection.

3.7. Step VII: Identifying Bandwidth and Duration of RFI

To characterize the bandwidth and duration of the L-band *RFI* contamination, MATLAB built-in functions "bwconncomp" and "regionprops" are used as shown in Figure 3. This approach is previously reported in [17] and implemented in this study without modifications. The "bwconncomp" function combines the neighboring MPD *RFI* flag samples (eight-connectivity) as single *RFI* signals occupying multiple time and frequency bins. Then, through the "regionprops" function, the bandwidth and duration of these *RFI* signals

were retrieved. This function, when used with the "BoundingBox" property, measures the dimensions of the smallest rectangle surrounding the *RFI* signal, and these dimensions correspond to the bandwidth and duration of the *RFI* signals. However, it is important to acknowledge the fact that this algorithm may unintentionally combine separate *RFI* sources with overlapping time and frequency bins if they are geographically close; thus, erroneously treat them as single *RFI* signals.

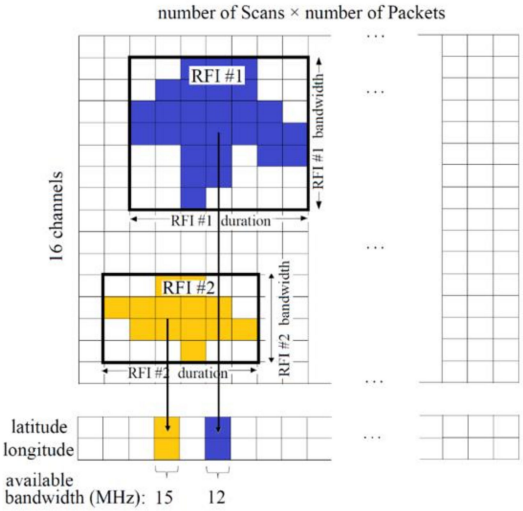

Figure 3. Extracting *RFI* properties using MATLAB's "bwconncomp" and "regionprops" functions on maximum probability of detection (MPD) *RFI* flags. In this example, two separate *RFI* sources (*RFI*#1 in blue and *RFI*#2 in yellow) were identified by the "bwconncomp" function, and the "regionprops" function provides their bandwidth (*RFI*#1 bandwidth = 7 × 1.5 MHz and *RFI*#2 bandwidth = 4 × 1.5 MHz) and duration (*RFI*#1 duration = 7 × 1.2 ms and *RFI*#2 duration = 6 × 1.2 ms). *SMAP* Level 1A data also include geolocation information, thus these *RFI* sources can be assigned to particular locations based on their mid-point in time.

3.8. Step VIII: Geo-Locating RFI Signals

Finally, *RFI* signals detected and characterized in previous steps are assigned to their geographical locations based on the latitude and longitude values of their middle points in time. This enables geo-located analyses of the L-band *RFI*, which has never been reported in detail so far.

4. Results and Discussion

RFI environment observed by the *SMAP* radiometer in the protected portion of L-band between 1 and 7 May 2019 has been characterized by processing its Level 1A data through the steps listed in the previous section in terms of the bandwidth and duration of *RFI* signals, availability of *RFI*-free bandwidth, and the distribution of the *RFI* contamination in each 1.5 MHz *SMAP* channel. The following sections discuss these *RFI* properties based on their geographic location and observation time.

4.1. Spectral Properties of L-Band RFI

Figure 4 illustrates the spectral properties of H-pol *RFI* contamination observed by *SMAP* across the world between 1 and 7 May 2019, in terms of maximum and mean bandwidth of *RFI* signals, average *RFI*-free spectrum available, and difference in maximum *RFI* bandwidths between ascending and descending *SMAP* orbits. V-pol characteristics are not shown here but were found to be very similar.

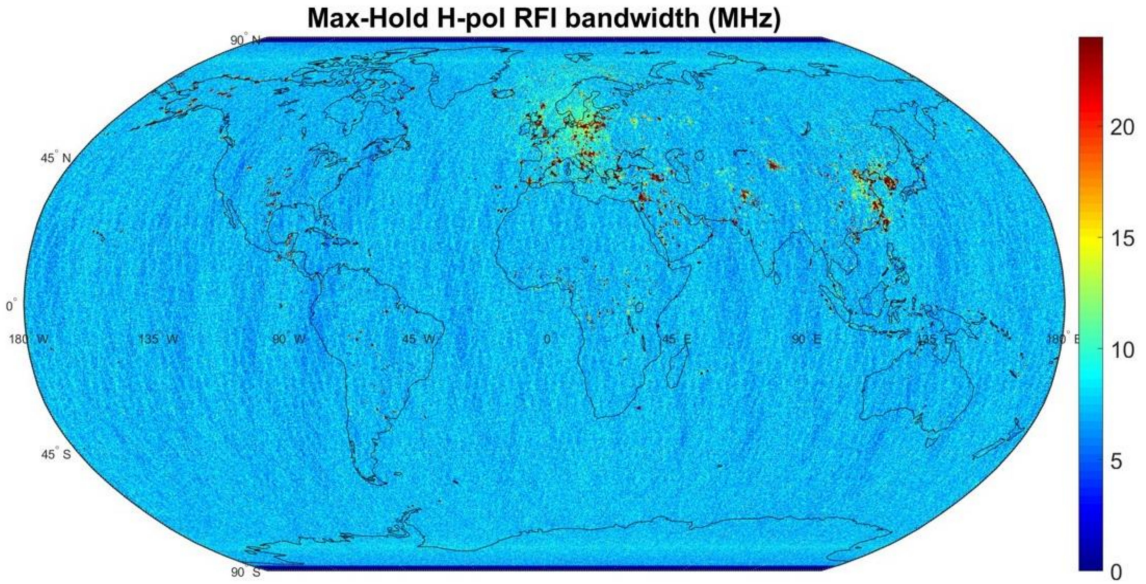

(**a**)

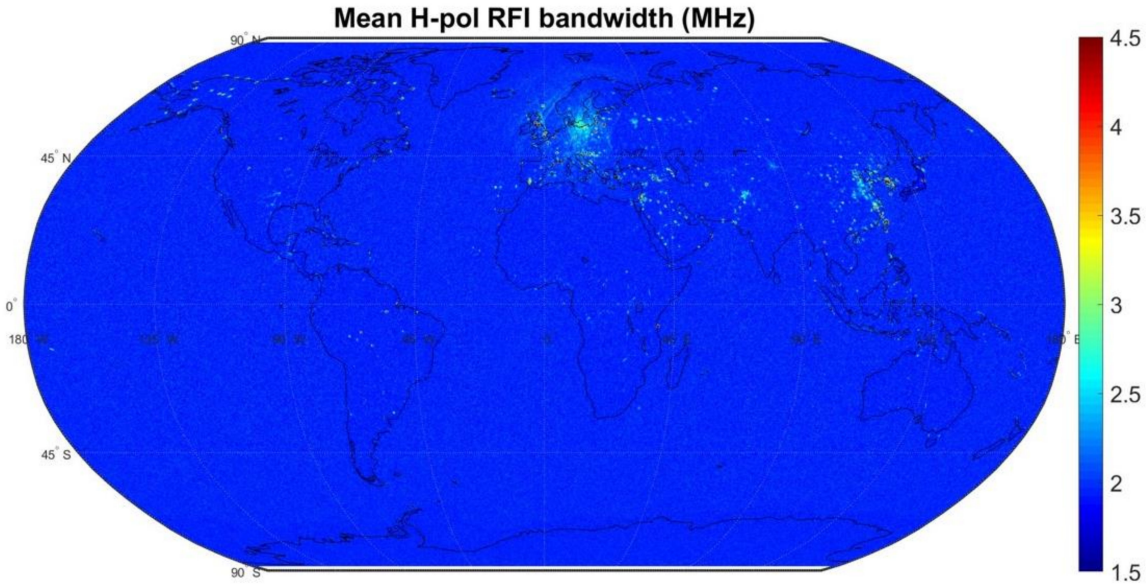

(**b**)

Figure 4. *Cont*.

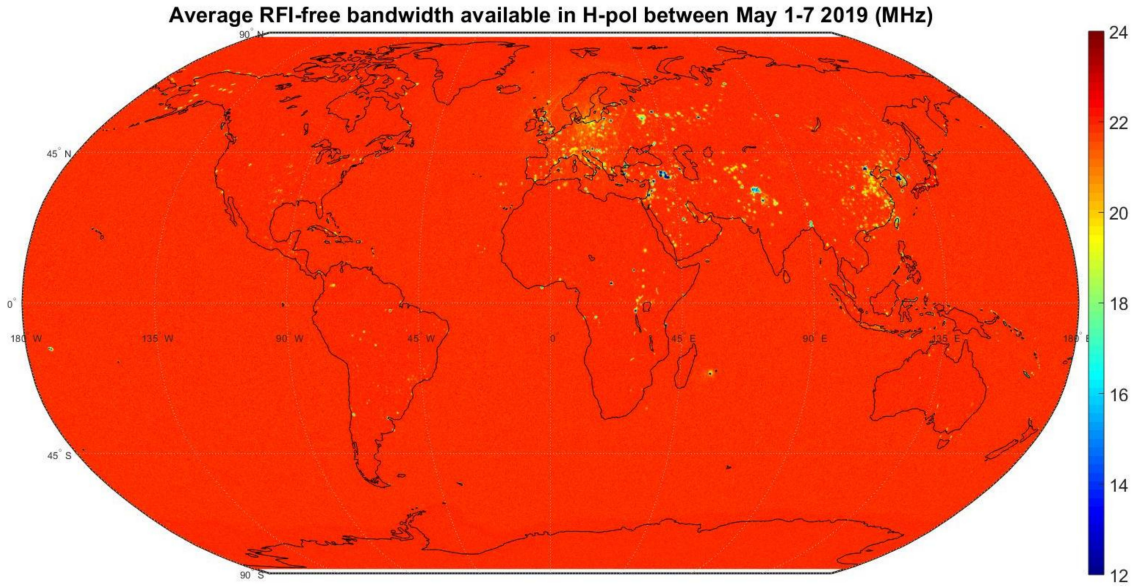

(**c**)

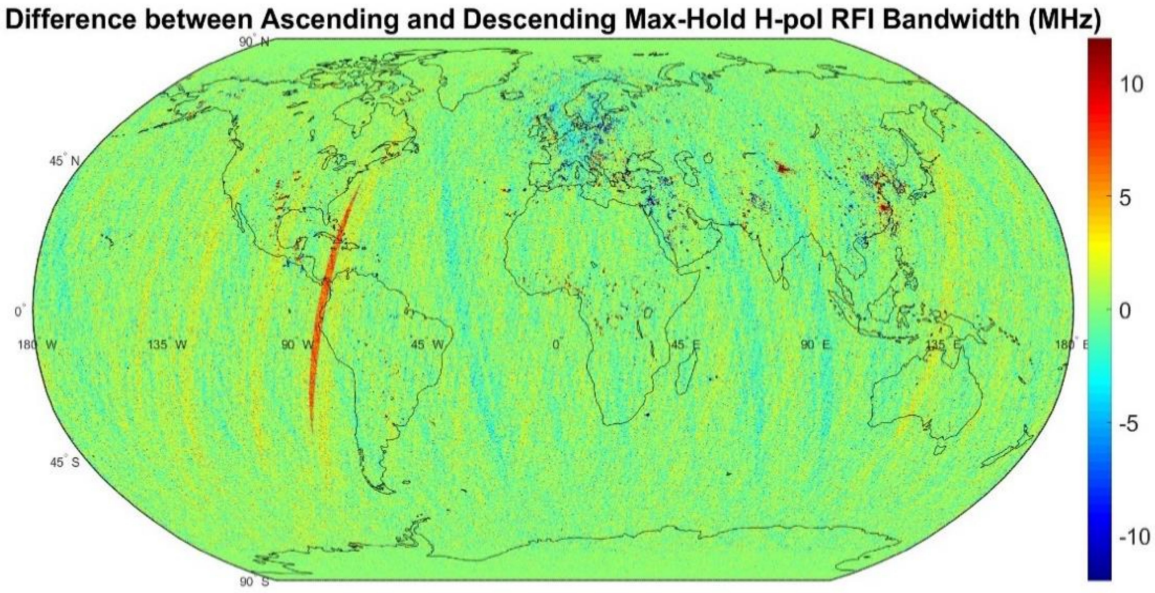

(**d**)

Figure 4. (**a**) Maximum *RFI* bandwidths, (**b**) average *RFI* bandwidths, (**c**) average *RFI*-free bandwidth availability (in MHz), and (**d**) difference in maximum *RFI* bandwidth between ascending and descending orbits within the *SMAP* band in H-pol between 1 and 7 May 2019 on 0.25° × 0.25° gridded maps. The large orange region in (**d**) is due to missing data in descending orbits.

As seen from the Figure 4a, the maximum *RFI* bandwidth varies up to 24 MHz, i.e., the entire *SMAP* band, and wideband *RFI* mostly appears in Korea, Eastern China, Central Asia, Middle East, and Europe. The average *RFI* bandwidth, depicted in Figure 4b, on the other hand, usually remains below 4.5 MHz except a few regions such as South Korea, Israel, and Northern England, which indicate continuous and widespread *RFI* contamination in these locations. The widespread *RFI* contamination in Northern Europe with maximum and average bandwidths of >10 and ~2.5–3 MHz, respectively, is also noteworthy. Figure 4c shows the average *RFI*-free spectrum available across the world. The average *RFI*-free bandwidth over a location, in this study, is defined as follows:

$$avg\{SMAP_{BW} - \cup RFI_{BW}\} \quad (4)$$

where $SMAP_{BW}$ denotes the entire *SMAP* bandwidth, i.e., 24 MHz, and $\cup RFI_{BW}$ is the bandwidth of the union of all *RFI* signals observed in that location. As seen from the figure, in general, this parameter seems to be larger than 18 MHz across the world. However, the *RFI*-free spectrum availability is very limited in some regions such as South Korea, Northern China, Central Asia, and South-Eastern Turkey.

Finally, differences in maximum *RFI* bandwidths between ascending and descending *SMAP* orbits may be significant as shown in Figure 4d. Both increases and decreases up to 10 MHz in *RFI* bandwidth are visible between the ascending and descending measurements in different locations, which is particularly noticeable over Eastern and Central Asia, Europe, and the Middle East. Note that the orange line in the figure that spreads over North-to-South America and indicates large bandwidth differences between ascending and descending orbits is a result of missing descending *SMAP* measurements over this region between 1 and 7 May 2019.

4.2. Temporal Properties of L-Band RFI

The temporal properties of L-band *RFI* contamination is described in terms of *RFI* duration. Figure 5 depicts the maximum and average durations of H-pol *RFI* signals observed by *SMAP* across the world between 1 and 7 May 2019, as well as the change in *RFI* durations between ascending and descending orbits. V-pol characteristics are not shown here but found to be very similar.

As seen from the figure, maximum *RFI* durations vary substantially based on location; but interference observed longer than 30 ms is not uncommon especially over Europe, the Middle East, and Central and Eastern Asia. These long-duration *RFI* signals occupy several *SMAP* footprints (one *SMAP* footprint is ~9.6 ms); thus, may not be detected efficiently by the *SMAP* time domain pulse blanking algorithm, which operates within single *SMAP* footprints.

Average *RFI* durations, usually below 4.8 ms, seem to be much shorter than the maximum values shown in Figure 5a, indicating spatially and temporally limited *RFI* contamination. These are also much shorter than duration of a *SMAP* footprint, which indicates, on average, *SMAP* time domain pulse blanking algorithms can detect such contamination efficiently. However, there are still a few locations suffering from longer-duration, persistent *RFI*, i.e., longer than one *SMAP* footprint, in Central Asia, South-Eastern Turkey, Moscow, and Reunion Island, and it is not surprising that as shown in Figure 1 some of these regions demonstrate *RFI* signatures even in *RFI*-free *SMAP* products. Finally, similar to the extensive wideband *RFI* corruption in Northern Europe, Northeastern China experiences widespread and relatively long-duration *RFI* corruption in L-band.

Moreover, similar to bandwidth, *RFI* durations are also varying considerably with time, between ascending and descending observations. Figure 5c illustrates this (again the large orange line is due to missing data in descending orbits), i.e., the difference in maximum *RFI* durations between ascending and descending *SMAP* orbits, which may be significant, up to ~10 ms, which is approximately one *SMAP* footprint, over Europe, Eastern and Central Asia, the Middle East, and Reunion Island. On the other hand, comparing Figures 4 and 5, one can conclude that the change in the temporal and spectral properties of the L-band *RFI* environment between ascending and descending measurements is not necessarily correlated. Moscow and Reunion Island, where only *RFI* durations change between ascending and descending observations, are examples of this observation.

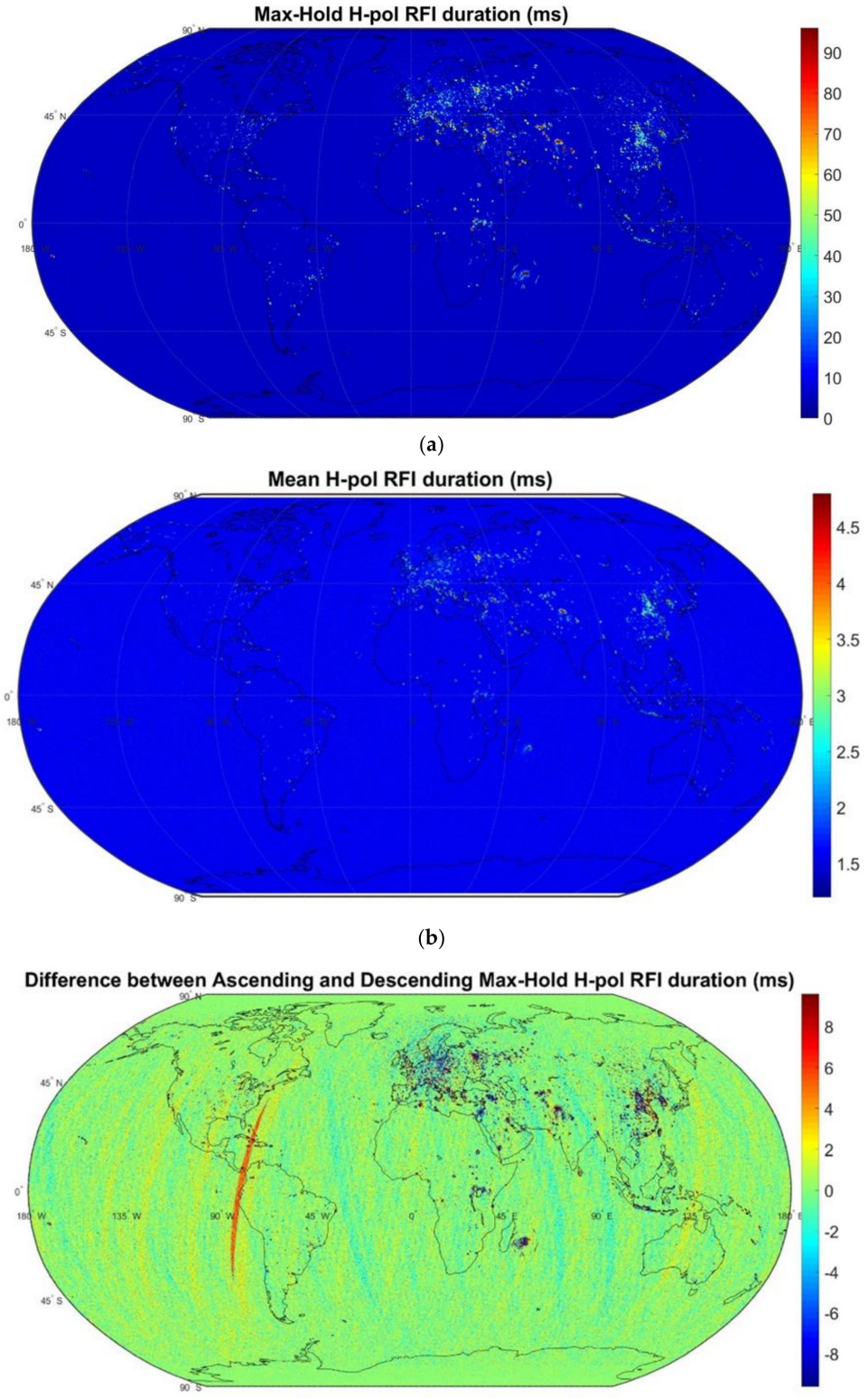

Figure 5. (**a**) Maximum *RFI* durations, (**b**) average *RFI* durations, and (**c**) difference in maximum *RFI* durations between ascending and descending orbits within the *SMAP* band in H-pol between 1 and 7 May 2019 on 0.25° × 0.25° gridded maps. The large orange region in (**c**) is due to missing data in descending orbits.

4.3. Spectral Distribution of L-Band RFI

Previous microwave radiometers operating in L-band such as Soil Moisture and Ocean Salinity (SMOS) [25–28] and Aquarius [29,30] have only one frequency channel occupying the protected portion of L-band; thus, it has not been possible to determine which frequencies within this spectrum are susceptible to *RFI* contamination. Due to its 16 × 1.5 MHz frequency channels, on the other hand, *SMAP* has enabled such analyses. This study defines the *RFI* percentage in a *SMAP* channel, $\%RFI_{ch}$, as follows:

$$\%RFI_{ch} = \frac{Ch_{flag}}{T_{flag}} \times 100 \quad (5)$$

where Ch_{flag} denotes the number of MPD *RFI* flags within that *SMAP* channel and T_{flag} is the number total MPD *RFI* flags in all 16 frequency channels. For instance, if *RFI* exists only in one *SMAP* channel over a region, $\%RFI_{ch}$ is 100 for that channel and 0 for all other channels over that area. On the other hand, if *RFI* contamination is equally distributed in all *SMAP* channels, then, $\%RFI_{ch}$ is 6.25% for all channels. Figures 6 and 7 show H-pol $\%RFI_{ch}$ for all *SMAP* frequency channels across the world (V-pol results are not shown here but found to be similar). These figures indicate that, contrary to popular belief, *RFI* contamination is not necessarily concentrated at the edges of the protected portion of L-band due to leakage from adjacent bands, as some strong *RFI* sources can be observed in 1409, 1410.5, 1412, 1413.5, and 1415 MHz channels. Over Northern Europe and Reunion Island, for example, $\%RFI_{ch}$ at these frequencies varies between 12 and 20. On the other hand, at the edges of the *SMAP* band, i.e., 1400/1424, 1401.5, and 1403 MHz, as well as 1421, and 1422.5 MHz, severe *RFI* contamination exists and $\%RFI_{ch}$ ranges from 10 to more than 20 over Central and Eastern Asia, Eastern Europe, North-Eastern Africa, and, especially in 1400/1424 and 1401.5 MHz channels, over Italy. Considering the overall worldwide *RFI* distribution across the *SMAP* channels given in [17], it is still expected that sum of *RFI* contamination within these channels constitutes the majority of L-band *RFI*.

4.4. Overall Worldwide Spectro-Temporal RFI Properties

Besides separate analyses of temporal and spectral properties of L-band *RFI* and their geographical distribution, a worldwide and cumulative joint analysis of these features is useful. Figure 8 shows the average *RFI* duration versus average *RFI* bandwidth observed by *SMAP* in horizontal polarization during its ascending and descending orbits between 1 and 7 May 2019 (V-pol results are not shown here but found to be similar). As seen from the figure, the average L-band *RFI* is mostly short (<9.6 ms) and narrowband (<5 MHz); however, significant number of cases with longer durations or wider bandwidths have also been observed. *RFI* signals with both long durations and wide bandwidths are particularly of interest to the microwave radiometry community as such noise-like interference cannot be easily detected by the traditional algorithms listed in Section 3. Another notable information Figure 8 presents is that, although a small correlation can be seen between *RFI* bandwidth and minimum *RFI* duration, i.e., the minimum *RFI* duration observed for a certain bandwidth increases with bandwidth itself, observed *RFI* durations and bandwidths are predominantly uncorrelated.

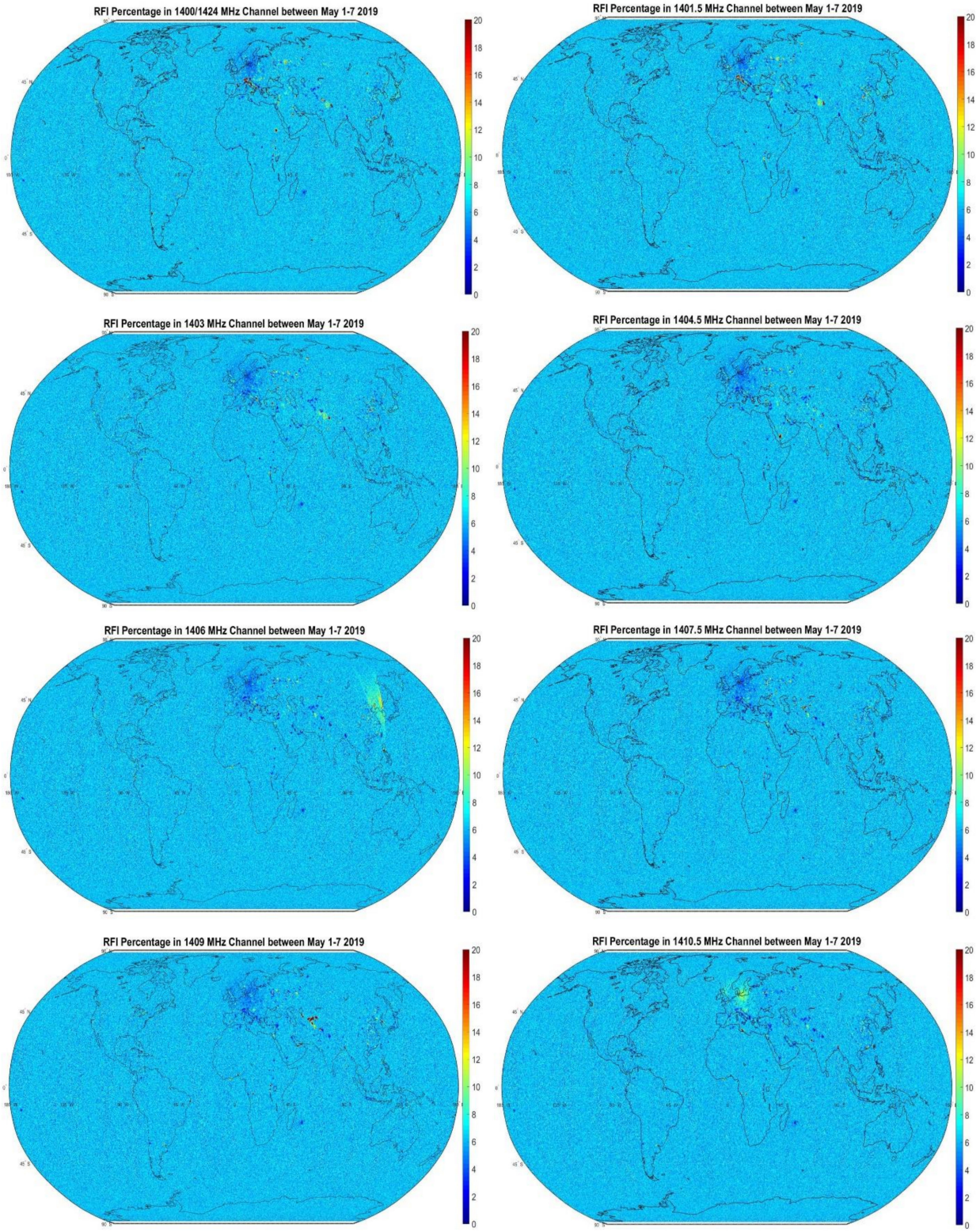

Figure 6. *RFI* percentage in 8 *SMAP* sub-band channels from 1400/1424 to 1410.5 MHz between 1 and 7 May 2019 on $0.25^\circ \times 0.25^\circ$ gridded maps. The background non-zero *RFI* percentage is due to false alarms in *RFI* detection. Note the significant *RFI* presence over Italy at 1400/1424 and 1401.5 MHz, over Eastern Asia at 1406 MHz, over Central Asia at 1409 MHz, and over Northern Europe at 1410.5 MHz.

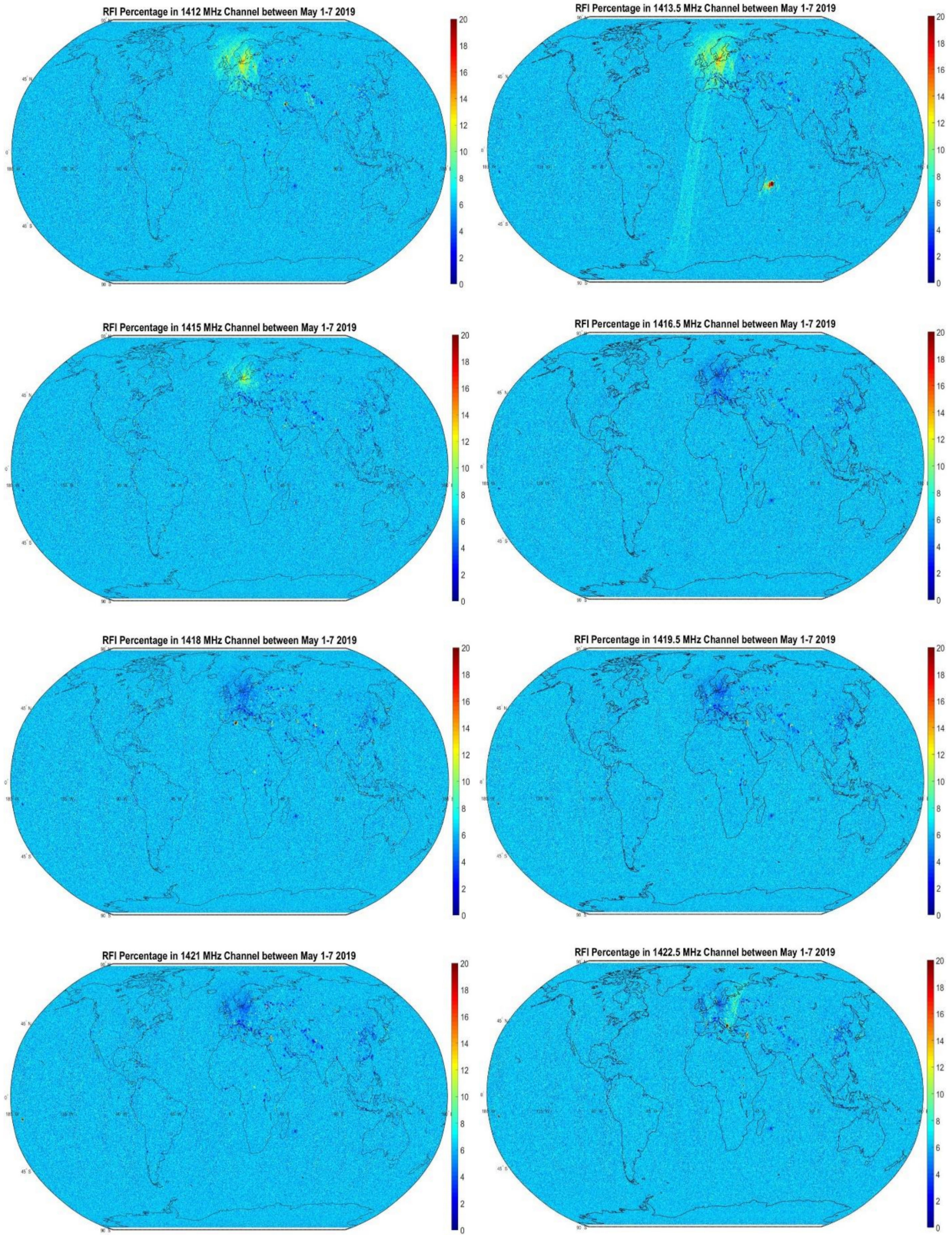

Figure 7. *RFI* percentage in 8 *SMAP* sub-band channels from 1412 to 1422.5 MHz between 1 and 7 May 2019 on 0.25° × 0.25° gridded maps. The background non-zero *RFI* percentage is due to false alarms in *RFI* detection. Note the significant *RFI* presence over Europe at 1412, 1413.5, and 1415 MHz, over Reunion Island at 1413.5 MHz, and over Eastern Europe and the Middle East at 1422.5 MHz.

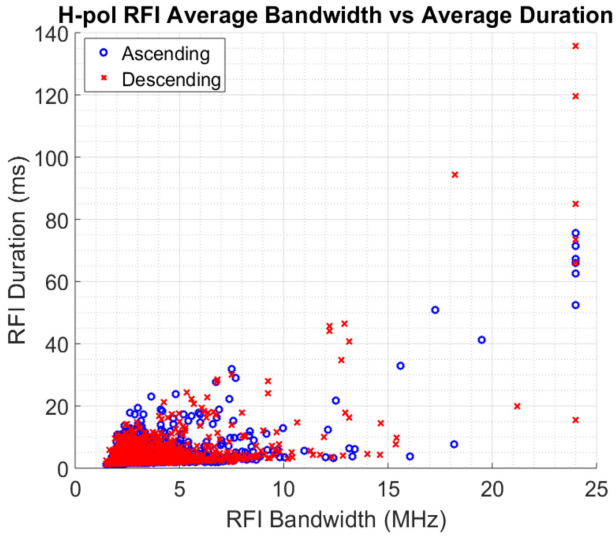

Figure 8. Bandwidth–duration characteristics of L-band H-pol *RFI* as observed by *SMAP* between 1 and 7 May 2019.

5. Conclusions and Discussion

This paper presents the geo-located temporal and spectral characteristics of *RFI* present in the protected portion of L-band. It has been shown that bandwidth, duration, and spectral distribution of L-band *RFI* may vary significantly with location and observation time, and there is no strong correlation between these features. Table 1 summarizes the overall results of this study regarding the temporal and spectral properties of L-band *RFI* as well as the amplitude information extracted from *SMAP* Level 1A and 1B data for each continent. Table 2, on the other hand, demonstrates the *RFI* contamination in each *SMAP* frequency channel to specify particular frequencies, which are not necessarily at the edges of the protected portion of L-band, susceptible to *RFI* over different locations.

The results of this study, indicating that temporal and spectral properties of L-band *RFI* may vary considerably with time and location, suggest that multi-domain comprehensive *RFI* detection algorithms supported by advanced digital backends, as implemented in *SMAP*, are good steps toward identifying and removing interference in radiometric measurements. On the other hand, to decrease false-alarm rates and data loss, dynamic weights and thresholds should be introduced to such algorithms, which can adjust the entire *RFI* detection and mitigation procedure based on time and location of the measurements. Machine learning and artificial intelligence methods, which are becoming popular recently in remote sensing applications [31–33], can be used to train radiometers as these instruments orbit the Earth to tune the *RFI* detection parameters in real time.

Finally, one should note that the performance of *RFI* detection and characterization algorithms applied in this study, and thus the durations and bandwidths presented in this paper, are constrained by *SMAP*'s 1.2 ms temporal, 1.5 MHz spectral, and ~40 km spatial resolutions. More capable radiometers in future spaceborne remote sensing missions with higher data sampling rates and spatial resolutions would reveal more accurate information regarding the L-band *RFI* characteristics. In addition, due to the substantial size of *SMAP* Level 1A data files, only one week of *SMAP* measurements were analyzed. *RFI* properties are known to change in time; but, although different time periods may demonstrate different characteristics, this one week was found to be enough to present the main conclusions of this study summarized in the previous paragraphs, i.e., (1) bandwidth, duration, and spectral distribution of L-band *RFI* may vary significantly with location and observation time, (2) *RFI* contamination is not limited to the edges of the protected portion of L-band, and (3) multi-domain comprehensive detection algorithms with dynamic weights and thresholds are required for proper *RFI* mitigation. Finally, the detection procedure described in Section 3 is not very efficient against wideband and long-duration, i.e., noise-like,

RFI contamination. For instance, over Japan, no L-band *RFI* was detected in this study although the region is known to be heavily *RFI* contaminated in L-band [34]. As more effective algorithms are developed against such noise-like *RFI*, they can be included in future studies to characterize the L-band *RFI* environment more precisely.

Table 1. L-band *RFI* properties over different continents.

***RFI* Properties**	**Africa**	**Asia**	**Europe**	**Americas**	**Oceania**
Amplitude	>50 K *RFI* over Reunion Island. Strong *RFI*, >50 K, over Sudan, South Sudan, DRC, Nigeria, and Algeria.	>50 K *RFI* mostly concentrated over discrete regions over Central Asia, the Middle East, and South-Eastern Asia. Widespread, >20K, *RFI* contamination over Eastern China.	Widespread, >20 K, *RFI* contamination over Northern Europe. Several discrete regions with >50 K *RFI* over Southern Europe.	Discrete >50 K *RFI* regions over Colombia and Cuba. Discrete locations in the U.S. and Brazil with 20–50 K *RFI*.	~15–20 K *RFI* near Melbourne.
Average Bandwidth	Discrete regions over Eastern Tanzania and Central African Rep. with >4.5 MHz bandwidth.	Wideband *RFI* over South Korea, Taipei, and Israel with >4.5 MHz bandwidth. 3–4.5 MHz bandwidth over Eastern China, Central Asia, and the Middle East.	Wideband *RFI* over UK and continental Europe with >4.5 MHz bandwidth. Widespread *RFI* over Northern Poland and Germany with 2.5–3.5 MHz bandwidth.	A few discrete locations in South America and Alaska with *RFI* bandwidth >4.5 MHz *RFI*.	*RFI* over Northern Australia with 2.5–3 MHz bandwidth.
Maximum Bandwidth	Discrete regions in Central Africa with *RFI* bandwidth up to 24 MHz.	*RFI* with up to 24 MHz bandwidth over Eastern China, South Korea, Central Asia, and the Middle East.	Several regions all over the continent with *RFI* bandwidth up to 24 MHz.	Regions in South America, Mexico, and Central U.S. with *RFI* bandwidth up to 24 MHz.	*RFI* with 24 MHz bandwidth over two locations in Northern Australia.
Average RFI-free Bandwidth	>20 MHz except few regions in Sudan, South Sudan, and DRC. <12 MHz over Reunion Island and regions in Eastern Tanzania and DRC.	>20 MHz except Eastern China, Central Asia, and the Middle East. Regions in South Korea, Northern China, and South-Eastern Turkey suffer from limited, <12 MHz, band availability.	Mostly >18 MHz all over the continent.	Mostly >20 MHz with discrete regions having 1–2 MHz-less *RFI*-free spectrum.	Mostly >20 MHz.
Difference in Maximum Bandwidth between Ascending and Descending Orbits	Ascending bandwidths are larger up to 10 MHz over discrete regions in Central Africa.	>10 MHz wider bandwidth in ascending then descending over Eastern China and Central Asia. ~10 MHz wider bandwidth in descending orbits over discrete locations in China, Northern India, and the Middle East	Descending bandwidths are usually 5–10 MHz larger in Central and Eastern Europe. Over the Balkans and Italy, discrete regions with ~10 MHz larger ascending bandwidths.	~10 MHz wider bandwidths in ascending orbits over certain locations Central and Southern U.S as well as Mexico.	No difference observed.

Table 1. *Cont.*

RFI Properties	Africa	Asia	Europe	Americas	Oceania
Average Duration	>4.5 ms over certain locations in Reunion Island, DRC, Sudan, South Sudan, and Algeria.	>4.5 ms over certain locations in South Korea, Central Asia, and the Middle East. Widespread *RFI* with ~2.5 ms duration over Northern China.	>4.5 ms over Moscow, Russia, and discrete locations in Southern Europe.	>4.5 ms over a location in Colombia.	*RFI* near Melbourne with ~2.5–3.5 ms duration.
Maximum Duration	>80 ms over locations in Reunion Island, Sudan, Nigeria, Algeria, and DRC.	>90 ms over locations in South Korea, Central Asia, and the Middle East. Widespread *RFI* with durations 30–50 ms.	>90 ms over locations in Central Russia, the Balkans, and Italy. Many more locations with 30–50 ms durations all over the continent.	>90 ms over a few locations in Colombia, Chile, and Argentina. 30–50 ms *RFI* over regions in Eastern U.S., California, and Brazil.	30–50 ms over discrete regions in South-Eastern Australia.
Difference in *RFI* Duration between Ascending and Descending Orbits	>8 ms difference over locations in Reunion Island, Algeria, Nigeria, Sudan, DRC, Uganda, and Kenya.	>8 ms difference over several regions in Eastern China, South Korea, Central and South-Eastern Asia, and the Middle East.	Widespread difference up to >8 ms all over the continent.	Discrete locations in North and South America with differences up to >8 ms.	No significant differences observed.

Table 2. *RFI* percentages ($\%RFI_{ch}$) in *SMAP* channels over different continents.

SMAP Channels	Africa	Asia	Europe	Americas	Oceania
1400/1424 MHz	>20 over certain regions in Sudan, South Sudan, Ethiopia, and Uganda.	>20 over regions in Central Asia, South-Eastern China, and the Middle East. ~10 over many other locations in Eastern China and the Middle East.	>20 over many regions in Italy, the Balkans, and Northern Spain. Widespread *RFI* with *RFI* percentage ~10 over Eastern Europe and Russia.	>20 over discrete regions in Colombia, Chile, and California.	No significant *RFI* observed.
1401.5 MHz	>20 over certain regions in South Sudan and Uganda.	>20 over a few regions in Northern India and Eastern China. ~10 over several locations in the Middle East and Central Asia.	>20 over many regions in Italy, Ukraine, Russia, and the tU.K. Several locations with *RFI* percentage ~10 over Eastern Europe and Russia.	>20 over discrete regions in Mexico, Chile, and California.	No significant *RFI* observed.
1403 MHz	>20 over locations in Algeria and Rwanda/Burundi.	>20 over regions in Central Asia, Turkey, and Eastern China. Widespread *RFI* with *RFI* percentage ~10 over Central Asia.	>20 over Albania and many locations in Russia. ~10 over several locations across the continent.	>20 over certain locations in Texas and California. ~12 over regions in Mexico and Chile.	No significant *RFI* observed.
1404.5 MHz	>20 over locations in Algeria.	>20 over Southern Saudi Arabia and Northern Yemen. 8–15 over several regions in Central Asia, India, and Turkey.	15–20 over several locations in Russia and Ukraine.	No significant *RFI* observed.	No significant *RFI* observed.

Table 2. *Cont.*

SMAP Channels	Africa	Asia	Europe	Americas	Oceania
1406 MHz	~15 over a coastal region near Ghana.	>20 over certain locations in the Philippines and Pakistan. Widespread *RFI* with *RFI* percentage 8–16 over China and Korea.	8–20 over discrete regions in Russia and the Balkans.	>20 over a region in Ecuador.	No significant *RFI* observed.
1407.5 MHz	12–20 over several locations in Ghana, Uganda, Rwanda/Burundi, and Congo.	>20 over many regions in Central Asia. 12–15 over several locations in China and Korea. ~12 over Sinai and Tajikistan.	>20 over regions in Southern Italy and Central Russia. 8–12 over many regions throughout the continent.	No significant *RFI* observed.	No significant *RFI* observed.
1409 MHz	>20 over locations in Nigeria, Uganda and Congo. 10–15 over regions in Rwanda/Burundi and Ghana.	>20 over several locations in Central Asia, Korea, and the United Arab Emirates. 8–12 over several locations in China, Korea, and Sinai.	>20 over a few regions in Northern Italy, Southern France, and Spain. 8–14 over several locations in Russia and continental Europe.	~20 over some locations in Brazil, Argentina, Cuba, and California.	No significant *RFI* observed.
1410.5 MHz	>20 over locations in Libya, Nigeria, Uganda, and Congo. 10–14 over some locations in Ghana and Rwanda/Burundi.	>20 over regions in Bangladesh, Pakistan, Hong Kong, and Taiwan. 8–14 over several location in Central Asia, China, Korea, and Sinai.	>20 over a few regions in Northern Italy, Southern France, and near Moscow. Widespread *RFI* with *RFI* percentage 10–12 over Northern and Central Europe.	~20 over some locations in Argentina.	No significant *RFI* observed.
1412 MHz	>20 over regions near Congo and Libya. ~12 over a location near Ghana.	>20 over several locations in Kuwait, Central Asia, Bangladesh, North-Eastern China, Caucasus, and Siberia. 8–12 over a large region in Pakistan and Afghanistan.	Widespread *RFI* over almost the entire continent with >8 *RFI* percentage. >20 over discrete regions in Russia.	15–20 over a few regions in Argentina and Brazil.	No significant *RFI* observed.
1413.5 MHz	Widespread *RFI* with *RFI* percentage >20 over Reunion Island. >20 over a location near Congo.	>20 over a few locations in Bangladesh, Central Asia, and Northern China. 8–12 over a few regions in Pakistan, China, and Korea.	Widespread *RFI* over almost the entire continent with >8 *RFI* percentage. >20 over discrete regions in Russia, Germany, and Sweden.	>20 over a few locations in Brazil.	No significant *RFI* observed.
1415 MHz	>20 over locations near Congo and Reunion Island.	~14 over certain regions in Saudi Arabia, Pakistan, and Bangladesh. 8–12 over several locations in the Middle East, Pakistan, China, and Korea.	Widespread *RFI* with *RFI* percentage 10–12 over Northern Europe. ~15 over several locations in Portugal, Russia, and Central Europe.	15–20 over several locations in New England, Chicago as well as in Argentina, Mexico, Peru, and Ecuador.	No significant *RFI* observed.
1416.5 MHz	10–12 over a few regions near Congo and Central African Republic.	8–20 over many regions in China, Korea, Central Asia, Iran, Saudi Arabia, and Siberia.	8–20 over several regions throughout the continent.	No significant *RFI* observed.	No significant *RFI* observed.

Table 2. *Cont.*

SMAP Channels	Africa	Asia	Europe	Americas	Oceania
1418 MHz	Large *RFI* with *RFI* percentage >20 over Algeria. 10–12 over some regions in Central Africa.	>20 over regions in Pakistan, Taiwan, Central Asia, Turkey, and Northern Japan. 8–14 over several regions in the Middle East, Siberia, China, and Central Asia.	>10 over many regions in Central and Eastern Europe, Greece, Southern Italy, Spain, and Portugal.	>20 over a few regions in New England, Northern U.S., and Canada.	>15 over a few discrete regions in Southern and Eastern Australia.
1419.5 MHz	10–14 over a few locations in Central Africa and South Sudan.	>12 over many regions in Turkey, the Middle East, Pakistan, Central Asia, and Siberia.	>8 over several discrete regions scattered over the continent.	No significant *RFI* observed.	~15 over a region in Eastern Australia.
1421 MHz	>20 over a few regions in Sudan, South Sudan, and near Libya. ~10 over a few regions in Central and Eastern Africa.	10–16 over several regions in China, the Middle East, Central Asia, and Siberia.	>8 over several discrete regions scattered over the continent.	>12 over discrete regions in Cuba as well as Northern and Eastern U.S.	No significant *RFI* observed.
1422.5 MHz	>20 over a few locations in Libya, Sudan, and South Sudan.	12–14 over many locations in the Middle East. ~20 over several regions in Myanmar, Bangladesh, and China. ~8–10 over scattered discrete regions.	>20 over a large area in the Balkans. >20 over discrete regions over Spain and Northern Europe. Widespread *RFI* over Eastern Europe with *RFI* percentage 8–10.	>14 over a region near the Great Lakes.	No significant *RFI* observed.

Author Contributions: Conceptualization, M.A.; methodology, M.A.; software, M.A. and H.R.; validation, M.A. and H.R.; formal analysis, M.A. and H.R.; investigation, M.A. and H.R.; resources, M.A. and H.R.; data curation, M.A. and H.R.; writing—original draft preparation, M.A. and H.R.; writing—review and editing, M.A., P.A., and I.M.N.; visualization, M.A. and H.R.; supervision, M.A.; project administration, M.A. All authors have read and agreed to the published version of the manuscript.

Funding: This research received no external funding.

Institutional Review Board Statement: Not applicable.

Informed Consent Statement: Not applicable.

Data Availability Statement: The data presented in this study are openly available in [19,21].

Acknowledgments: *SMAP* Level 1A and Level 1B data were obtained from the NASA Distributed Active Archive Center at the National Snow and Ice Data Center (NSIDC) [19,21].

Conflicts of Interest: The authors declare no conflict of interest.

References

1. National Research Council. *Handbook of Frequency Allocations and Spectrum Protection for Scientific Uses*; The National Academies Press: Washington, DC, USA, 2007.
2. Aksoy, M.; Johnson, J.T. A Comparative Analysis of Low-Level Radio Frequency Interference in SMOS and Aquarius Microwave Radiometer Measurements. *IEEE Trans. Geosci. Remote Sens.* **2013**, *51*, 4983–4992. [CrossRef]
3. Aksoy, M.; Johnson, J.T. A Study of SMOS *RFI* Over North America. *IEEE Geosci. Remote Sens. Lett.* **2013**, *10*, 515–519. [CrossRef]
4. Lahtinen, J.; Uusitalo, J.; Ruokokoski, T.; Ruoskanen, J. Evaluation and comparison of *RFI* detection algorithms. In Proceedings of the 2016 14th Specialist Meeting on Microwave Radiometry and Remote Sensing of the Environment (MicroRad), Espoo, Finland, 11–14 April 2016; pp. 62–67.

5. Niamsuwan, N.; Johnson, J.T.; Ellingson, S.W. Examination of a simple pulse-blanking technique for radio frequency interference mitigation. *Radio Sci.* **2005**, *40*, 1–11. [CrossRef]
6. Güner, B.; Johnson, J.T.; Majurec, N. Performance analysis of a cross-frequency detector of pulsed sinusoidal *RFI* in Mi-crowave Radiometry. In Proceedings of the 2009 IEEE International Geoscience and Remote Sensing Symposium, Cape Town, South Africa, 12–17 July 2009.
7. Tarongi, J.M.; Camps, A. Normality Analysis for *RFI* Detection in Microwave Radiometry. *Remote Sens.* **2009**, *2*, 191–210. [CrossRef]
8. Güner, B.; Frankford, M.T.; Johnson, J.T. A Study of the Shapiro–Wilk Test for the Detection of Pulsed Sinusoidal Radio Frequency Interference. *IEEE Trans. Geosci. Remote Sens.* **2009**, *47*, 1745–1751. [CrossRef]
9. Bradley, D.; Morris, J.M.; Adali, T.; Johnson, J.T.; Aksoy, M. On the detection of *RFI* using the complex signal kurtosis in microwave radiometry. In Proceedings of the 2014 13th Specialist Meeting on Microwave Radiometry and Remote Sensing of the Environment (MicroRad), Pasadena, CA, USA, 24–27 March 2014; pp. 33–38.
10. De Roo, R.D. A Simplified Calculation of the Kurtosis for *RFI* Detection. In Proceedings of the IGARSS 2008–2008 IEEE International Geoscience and Remote Sensing Symposium, Boston, MA, USA, 9 October 2008; pp. 3755–3760.
11. Kristensen, S.S.; Balling, J.; Skou, N.; Sobjoerg, S.S. *RFI* in SMOS data detected by polarimetry. In Proceedings of the 2012 IEEE International Geoscience and Remote Sensing Symposium, Munich, Germany, 22–27 July 2012; pp. 3320–3323.
12. Soldo, Y.; Le Vine, D.M.; Bringer, A.; Mohammed, P.N.; De Matthaeis, P.; Piepmeier, J.R.; Johnson, J.T. Recent Advances in *SMAP RFI* Processing. In Proceedings of the IGARSS 2018–2018 IEEE International Geoscience and Remote Sensing Symposium, Valencia, Spain, 22–27 July 2018; pp. 313–315.
13. Entekhabi, D.; Njoku, E.; O'Neill, P.; Spencer, M.; Jackson, T.; Entin, J.; Im, E.; Kellogg, K. The soil moisture active/passive mission (*SMAP*). In Proceedings of the IGARSS 2008–2008 IEEE International Geoscience and Remote Sensing Symposium, Boston, MA, USA, 7–11 July 2008.
14. Entekhabi, D.; Njoku, E.; O'Neill, P. The soil moisture active and passive mission (*SMAP*): Science and applications. In Proceedings of the 2009 IEEE Radar Conference, Pasadena, CA, USA, 4–8 May 2009; pp. 1–3.
15. Piepmeier, J.R.; Johnson, J.T.; Mohammed, P.N.; Bradley, D.; Ruf, C.; Aksoy, M.; Garcia, R.; Hudson, D.; Miles, L.; Wong, M. Radio-Frequency Interference Mitigation for the Soil Moisture Active Passive Microwave Radiometer. *IEEE Trans. Geosci. Remote Sens.* **2014**, *52*, 761–775. [CrossRef]
16. Mohammed, P.N.; Aksoy, M.; Piepmeier, J.R.; Johnson, J.T.; Bringer, A. *SMAP* L-Band Microwave Radiometer: *RFI* Miti-gation Prelaunch Analysis and First Year On-Orbit Observations. *IEEE Trans. Geosci. Remote Sens.* **2016**, *54*, 6035–6047. [CrossRef]
17. Rajabi, H.; Aksoy, M. Characteristics of the L-Band Radio Frequency Interference Environment Based on *SMAP* Radiom-eter Observations. *IEEE Geosci. Remote Sens. Lett.* **2019**, *16*, 1736–1740. [CrossRef]
18. Aksoy, M.; Rajabi, H. Characteristics of radio frequency interference in the protected portion of L-Band. In Proceedings of the IGARSS 2019–2019 IEEE International Geoscience and Remote Sensing Symposium, Yokohama, Japan, 28 July–2 August 2019; pp. 4539–4542.
19. *SMAP* L1A Radiometer Time-Ordered Parsed Telemetry, Version 2. National Snow and Ice Data Center. 2019. Available online: https://nsidc.org/data/SPL1AP/versions/2 (accessed on 1 June 2019).
20. Piepmeier, J. *SPL1AP/BTB Algorithm Theoretical Basis Document Version 2*; NASA: Washington, DC, USA, 2016.
21. *SMAP* L1B Radiometer Half-Orbit Time-Ordered Brightness Temperatures, Version 4\National Snow and Ice Data Center. Available online: https://nsidc.org/data/SPL1BTB/versions/4 (accessed on 1 June 2019).
22. Aksoy, M. Radio Frequency Interference Characterization and Detection in L-Band Microwave Radiometry. Ph.D. Thesis, The Ohio State University, Columbus, OH, USA, 2015.
23. De Roo, R.D.; Misra, S.; Ruf, C.S. Sensitivity of the Kurtosis Statistic as a Detector of Pulsed Sinusoidal *RFI*. *IEEE Trans. Geosci. Remote Sens.* **2007**, *45*, 1938–1946. [CrossRef]
24. Mach, P.; Hochlova, H. Testing of normality of data files for application of SPC tools. In Proceedings of the 27th International Spring Seminar on Electronics Technology: Meeting the Challenges of Electronics Technology Progress, Bankya, Bulgaria, 13–16 May 2004; pp. 318–321.
25. Kerr, Y.H.; Waldteufel, P.; Wigneron, J.-P.; Martinuzzi, J.; Font, J.; Berger, M. Soil moisture retrieval from space: The Soil Moisture and Ocean Salinity (SMOS) mission. *IEEE Trans. Geosci. Remote Sens.* **2001**, *39*, 1729–1735. [CrossRef]
26. Bindlish, R.; Jackson, T.J.; Piepmeier, J.R.; Yueh, S.; Kerr, Y. Intercomparison of *SMAP*, SMOS and Aquarius L-band brightness temperature observations. In Proceedings of the 2016 IEEE International Geoscience and Remote Sensing Symposium (IGARSS), Beijing, China, 10–15 July 2016; pp. 2043–2046.
27. Font, J.; Camps, A.; Borges, A.; Martín-Neira, M.; Boutin, J.; Reul, N.; Kerr, Y.H.; Hahne, A.; Mecklenburg, S. SMOS: The Challenging Sea Surface Salinity Measurement From Space. *Proc. IEEE* **2009**, *98*, 649–665. [CrossRef]
28. Johnson, J.T.; Aksoy, M. Studies of radio frequency interference in SMOS observations. In Proceedings of the 2011 IEEE International Geoscience and Remote Sensing Symposium, Vancouver, BC, Canada, 24–29 July 2011; pp. 4210–4212.
29. Ruf, C.; Chen, D.; Le Vine, D.M.; De Matthaeis, P.; Piepmeier, J. Aquarius radiometer *RFI* detection, mitigation and impact assessment. In Proceedings of the 2012 IEEE International Geoscience and Remote Sensing Symposium, Munich, Germany, 22–27 July 2012; pp. 3312–3315.
30. Le Vine, D.; De Matthaeis, P.; Ruf, C.; Chen, D.; Dinnat, E. Aquarius *RFI* detection and mitigation. In Proceedings of the 2013 IEEE International Geoscience and Remote Sensing Symposium—IGARSS, Melbourne, Australia, 21–26 July 2013; pp. 1798–1800.

31. Zerrouki, N.; Harrou, F.; Sun, Y.; Hocini, L. A Machine Learning-Based Approach for Land Cover Change Detection Using Remote Sensing and Radiometric Measurements. *IEEE Sens. J.* **2019**, *19*, 5843–5850. [CrossRef]
32. Sun, C.; Neale, C.M.U.; McDonnell, J.J.; Cheng, H.-D. Snow classification from SSM/I data over varied terrain using an artificial neural network classifier. In Proceedings of the IGARSS '96. 1996 International Geoscience and Remote Sensing Symposium, Lincoln, NE, USA, 31 May 1996; Volume 1, pp. 133–135.
33. Chai, S.; Veenendaal, B.; West, G.; Walker, J.P. Explicit Inverse of Soil Moisture Retrieval with an Artificial Neural Net-work Using Passive Microwave Remote Sensing Data. In Proceedings of the IGARSS 2008–2008 IEEE International Geoscience and Remote Sensing Symposium, Boston, MA, USA, 7–11 July 2008.
34. Soldo, Y.; De Matthaeis, P.; Le Vine, D. L-band *RFI* in Japan. In Proceedings of the 2016 Radio Frequency Interference (*RFI*), Socorro, NM, USA, 17–20 October 2016; pp. 111–114.